Screening of bimetallic electrocatalysts for water purification with machine learning

Richard Tran, Duo Wang, Ryan Kingsbury, et al.

COLLECTIONS

View Online   Export Citation   CrossMark

Screening of bimetallic electrocatalysts for water purification with machine learning

Richard Tran,[1] [iD] Duo Wang,[2] Ryan Kingsbury,[2] [iD] Aini Palizhati,[1] Kristin Aslaug Persson,[3,4] Anubhav Jain,[2] [iD] and Zachary W. Ulissi[1,a)] [iD]

AFFILIATIONS

[1] Department of Chemical Engineering, Carnegie Mellon University, Pittsburgh, Pennsylvania 15213, USA
[2] Lawrence Berkeley National Laboratory, Berkeley, California 94720, USA
[3] Department of Materials Science and Engineering, University of California Berkeley, Berkeley, California 94720, USA
[4] Molecular Foundry, Lawrence Berkeley National Laboratory, Berkeley, California 94720, USA

Note: This paper is part of the 2022 JCP Emerging Investigators Special Collection.
[a)] Author to whom correspondence should be addressed: zulissi@andrew.cmu.edu

ABSTRACT

Electrocatalysis provides a potential solution to NO_3^- pollution in wastewater by converting it to innocuous N_2 gas. However, materials with excellent catalytic activity are typically limited to expensive precious metals, hindering their commercial viability. In response to this challenge, we have conducted the most extensive computational search to date for electrocatalysts that can facilitate NO_3^- reduction reaction, starting with 59 390 candidate bimetallic alloys from the Materials Project and Automatic-Flow databases. Using a joint machine learning- and computation-based screening strategy, we evaluated our candidates based on corrosion resistance, catalytic activity, N_2 selectivity, cost, and the ability to synthesize. We found that only 20 materials will satisfy all criteria in our screening strategy, all of which contain varying amounts of Cu. Our proposed list of candidates is consistent with previous materials investigated in the literature, with the exception of Cu–Co and Cu–Ag based compounds that merit further investigation.

Published under an exclusive license by AIP Publishing. https://doi.org/10.1063/5.0092948

I. INTRODUCTION

The production of ammonia in large-scale agricultural processes came with the unforeseen consequences of an excess of nitrate (NO_3^-) by-products.[1–3] This results in NO_3^- runoff being one of the leading sources of surface and groundwater pollution. When left untreated, NO_3^- pollution can lead to significant damage to the surrounding ecosystem via eutrophication and have dire consequences for human health, such as methemoglobinemia in infants.[4] The removal of anthropogenic NO_3^- pollutants is essential to closing the nitrogen cycle in order to avoid further damage to human health and the environment.

Several methods exist to either remove NO_3^-, such as reverse osmosis,[5] oxo-anion adsorption,[6] and ion exchange,[7] or transform it into more benign by-products via chemical NO_3^- reduction[8–10] and biological degradation.[11–13] Although these technologies can be highly effective, with NO_3^- removal rates of up to 90%, each carries notable drawbacks. For example, chemical treatments require

constant replenishment of reactants, such as aluminum or hydrogen, and reverse osmosis has high capital and operation costs (especially if NO_3^- is the only pollutant of concern), and biological degradation processes may not perform well in colder climates and produce biological waste products that require further treatment. The most widely used process, i.e., ion exchange, requires periodic regeneration, which consumes significant chemical inputs and generates a highly concentrated brine waste that must be disposed or treated.[14] Both reverse osmosis and ion exchange only serve to remove and store NO_3^- in temporary waste reservoirs that require further processing.[15]

Electrocatalysis provides an alternative solution toward removing NO_3^- through an electrochemical reduction reaction (NO_3^-RR).[16] Unlike in ion exchange, a catalyst does not require regeneration. Furthermore, NO_3^-RR transforms NO_3^- into benign by-products that stem from the available reaction pathways rather than storing it in excess brine solutions or biological wastes, reducing the cost of subsequent water treatments. Factors such as

the catalyst, applied potential, acidity, and reducing agent can be adjusted to control the selectivity and activity.[17,18] For example, Rh has higher activity for NO_3^-RR when compared to other platinum group metals.[19] Meanwhile, the use of NaCl and Na_2SO_4 solutions as the electrolyte for a Pt catalyst demonstrated increased efficiency for NO_3^- removal. The NaCl solution, in particular, demonstrated an increase in selectivity toward N_2, a desired by-product in water purification that safely dissipates back into the air.[20]

Despite the clear advantages, a major concern in the economic viability of electrocatalytic NO_3^-RR lies in the cost of the catalyst. The most commonly used electrocatalysts are rare and expensive metals such as palladium and platinum and their alloys, which have demonstrated excellent activity for electrochemical NO_3^-RR in water.[18] The use of precious metals drastically increases the material cost of electrocatalysis with the recent costs (as of April 30, 2021) of Pt and Pd ranging up to \$38 694/kg and \$79 855/kg, respectively.[21] The search for catalysts composed of cheap earth-abundant metals with high activity and selectivity is, therefore, crucial for the commercial viability of electrocatalytic NO_3^-RR.

Computational screening can potentially be used to identify catalytically and commercially viable materials. Recently, computational screening has grown in popularity as a quick and efficient tool for identifying heterogeneous catalysts based on a series of criteria used to screen desired properties.[22–26] Singh et al.,[22] for example, were able to identify 52 potential photocatalysts for CO_2 reduction using simple thermodynamic and electronic properties. However, the high computational cost renders the explicit assessment of catalytic activity and selectivity in candidate materials impractical in these strategies.

Typically, these properties are calculated using microkinetic modeling in conjunction with first-principles calculation methods, such as density functional theory (DFT).[27–30] Using the reaction rates of elementary steps (i.e., activation and reaction energies, E_{act} and E_{rxn}), microkinetic models can determine the activity and selectivity of material surfaces.[31] Typically, E_{act} and E_{rxn} are calculated with the expensive nudged elastic band (NEB) method. However, Brønsted–Evans–Polanyi (BEP) relations demonstrate that E_{act} and E_{rxn} can linearly scale as a function of the adsorption energies (E_{ads}) of intermediates, which can be determined with relatively inexpensive DFT calculations. This scaling relationship can be exploited to construct activity and selectivity models described by E_{ads} instead of E_{act} and E_{rxn}. Previous screening strategies have used such models to incorporate activity and selectivity criteria[23,24,26] to identify viable catalysts.

Recently, Liu et al.[32] were able to construct such a model for the activity of NO_3^-RR and by-product selectivity as a function of the adsorption energies of O and N (E_{ads}^{O*} and E_{ads}^{N*}). Although the model was constructed using the limited adsorption energies of elemental transition metal surfaces, the predictive capabilities of these descriptors were extended to screen several binary intermetallics with a Pt–Ru based compound demonstrating excellent activity toward NO_3^-RR. A subsequent joint experimental and computational study by Wang et al.[33] validated the catalytic activity for Pt doped with varying concentrations of Ru with $Pt_{0.78}Ru_{0.22}$, exhibiting the activity for NO_3^-RR on par with Rh.

These models can potentially be used to perform large data-driven screening of materials with the hope of identifying cheap earth-abundant electrocatalysts. However, the computational cost

of E_{ads}^{O*} and E_{ads}^{N*} using DFT is still impractical given the number of materials, facets, and surface-adsorbate configurations that exist, the combination of which would require millions of DFT calculations. A predictive model for E_{ads} is necessary if such a large-scale screening exercise is feasible. Recently, Chanussot et al., implemented the Open Catalyst Project[34] (OCP), a framework developed with the purpose of using machine learning (ML) to construct such models. The OCP dataset contains over 872 000 adsorption energies calculated with DFT across 55 adsorbates and 27 775 inorganic materials. Combining this training dataset with state-of-the-art graph neural network (GNN)[35] models allowed for the construction of predictive ML models generalized across any adsorbate and material surface with mean absolute errors (MAE) as low as 0.3 eV. The model is then able to determine the adsorption energy based on the initial unrelaxed geometries of an adsorbed slab. The small MAE and generality of these models can be used to screen the activity and selectivity of large material datasets based on the ML values for E_{ads}^{O*} and E_{ads}^{N*}.

In this article, we present a data-driven screening framework to accelerate our search for earth-abundant electrocatalysts for NO_3^-RR. We assessed the technical and commercial viability of materials based on their resistance to corrosion, activity for NO_3^-RR, N_2-selectivity, material cost,[15] and thermodynamic stability. We began our search by screening all symmetrically distinct binary transition metal alloys from the Materials Project (MP)[36] and Automatic-Flow (AFLOW)[37] databases, which yielded 59 390 materials. By leveraging the ML models for E_{ads} developed in the OCP and the models for activity and selectivity developed by Liu et al.,[32] we quickly and inexpensively estimated the catalytic capabilities of these materials. Through a series of progressive criteria, our screening pipeline has revealed 20 materials that satisfied all the requirements for commercial viability. Furthermore, we were able to qualitatively demonstrate that the compositional selection of catalytically active materials from our screening pipeline is consistent with previous experimental and computational observations.

II. APPROACH

A. Slab generation

We described all surfaces considered in this work with a slab model containing an atomic and vacuum layer of 8 and 20 Å thick, respectively. We considered the surfaces of 12 randomly selected and symmetrically distinct Miller index (hkl) planes with a maximum index of 3. We expanded our search to all (hkl) planes with a maximum index of 4 when investigating the final set of candidate materials. We excluded slabs that exceeded 250 atoms to avoid subsequent intense usage of computational resources. To avoid periodic interactions between the monatomic adsorbates, all slabs were expanded along the length and width to at least 8 Å. We, then, identified the adsorption sites for monatomic O and N on the surfaces using the method described by Montoya and Persson.[38]

B. DFT calculation parameters

All DFT energy calculations were performed using the Vienna *Ab initio* Simulation Package (VASP)[39,40] within the projector

augmented wave (PAW)[41] approach. The exchange–correlation effects were modeled using the Perdew–Berke–Ernzerhof (PBE) generalized gradient approximation (GGA)[42] functional to be consistent with the work performed by Liu *et al.*[32] All slab and bulk calculations were performed without spin-polarization except when Fe, Ni, and Co were present. The external electrons were expanded in plane waves with kinetic energy cutoffs of 400 eV. The energies and atomic forces of all calculations were converged to within 1×10^{-4} eV and 0.02 eV Å^{-1}, respectively. The Methfessel–Paxton method[43] was chosen as the smearing algorithm. We used Γ-centered k-point meshes of $\frac{35}{a} \times \frac{35}{b} \times \frac{35}{c}$ and $\frac{35}{a} \times \frac{35}{b} \times 1$ for bulk and slab calculations, respectively, with non-integer values rounded up to the nearest integer.

In all DFT calculations and ML predictions of E_{ads}^{O*} and E_{ads}^{N*}, we used the total energy of an isolated O and N atom, respectively, in a $16 \times 16 \times 16$ Å^3 box as the adsorbate reference energy.

All VASP input generation, slab modeling, adsorbate placement, thermodynamic, and cost analysis were performed using the Python Materials Genomics (pymatgen) package.[38,44,45]

C. Validation of machine learning and DFT

The OCP allows us to predict the relaxed adsorption energies of O and N from the initial structure of any intermetallic slab (IS2RE). Consolidating the IS2RE model with existing adsorption energy-based activity and selectivity maps allows us to efficiently infer the catalytic capabilities of large material datasets without the need of any DFT calculations. In this work, we adopted a modified implementation of the Directional Message Passing Neural Network (DimeNet++)[58,59] model. DimeNet improves upon GNN models by accounting for directional information in triplets of atoms via bond angles and interatomic distances. The improvements developed by Klicpera *et al.*[58] modifies to the hidden layers of the neural network to improve upon the runtime speeds and accuracy of DimeNet. Under the OCP, we adapted the DimeNet++ model for slabs by introducing a periodic boundary condition when constructing the graph. We considered all interatomic interactions within a cutoff radius of 6 Å, which under 256 hidden channels will yield 1.8×10^6 parameters. For a complete list of all other hyperparameters, we direct the reader to Table S4 from the reference herein.[34] We used this GNN model to predict E_{ads}^{O*} and E_{ads}^{N*}.

The training dataset from OCP is composed of adsorption energies calculated using the revised PBE (rPBE) functional, which is in contrast to the activity and selectivity maps built using the PBE functional.[32] We trained and validated the machine learning model with a subset of the Open Catalyst 2020 (OC20) dataset with a train/validation split of 183 075/9888,[34] and then tested using PBE data from this work to be consistent with Liu *et al.*[32] Our train/validation subset of the OC20 dataset contained 202 metallic, 1829 binary, and 2030 ternary intermetallic crystals queried from the Materials Project[36] with 82 different adsorbates (see Ref. 34). The adsorption energy dataset was constructed by randomly sampling low-Miller-index facets from the available intermetallics and adsorbates.

For our test set, we used DFT to calculate 59 additional data points for E_{ads}^{N*} and E_{ads}^{O*} of 30 Pourbaix stable compounds at randomly chosen facets with a maximum Miller index of 3. We also included the 52 data points from Liu *et al.*[32] for the binary intermetallics with Miller indices of (310) and (211) for the body and

face centered cubic crystals, respectively. Figure 1 plots the DFT calculated data points against the corresponding ML quantities with triangular data points obtained from Ref. 32. R^2 of the test set is 0.85, indicating a strong linear correlation between the DFT and ML quantities. The test set MAE is 0.35 eV, which is consistent with the MAE of 0.3 eV obtained from the validation set. Both the linear fit for E_{ads}^{*N} and E_{ads}^{*O} demonstrate a slope close to unity with the ML quantities for E_{ads}^{*O} consistently underestimating the DFT calculated quantities by 0.39 eV, while the ML quantities for E_{ads}^{*N} overestimates by 0.22 eV. The difference in functionals and the inherent MAE of 0.3 eV in the Dimenet++ model is possibly responsible for the offset of 0.39 eV in the ML values of E_{ads}^{*O}. This is in contrast to previous reports of the rPBE functional overestimating PBE by 0.1 eV in regard to adsorption energy.[60] Many materials and Miller indices sampled in the test set were out-of-domain from the training and validation sets. The strong linear correlation and consistent MAE with this out-of-domain test set indicates that our model is generalized for any intermetallic material and facet. Since the offset for E_{ads}^{*O} exceeds the expected MAE, we accounted for any disparity between the ML and DFT quantities by adding 0.39 eV to all ML quantities of E_{ads}^{*O}.

Next, we assess the predictability of the DFT inferred catalytic performance using the computed TOF as our primary metric. Here, we qualitatively compared previous experimental trends in catalytic performance across different metals and alloys to the trends in log(TOF) observed by Liu *et al.*[32] in their calculations. Figure 2 plots the range of log(TOF) inferred from the DFT calculated E_{ads}^{O*}
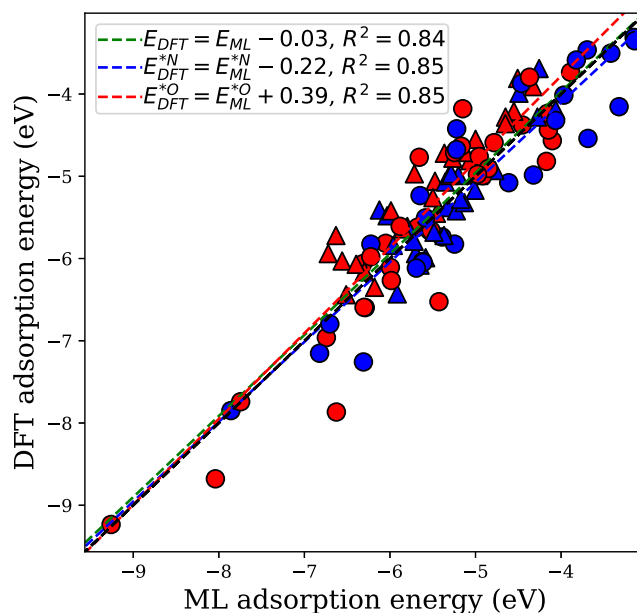

FIG. 1. Plot of E_{ads}^{*N} and E_{ads}^{*O} (blue and red, respectively) with DPP machine learning results on the x-axis and corresponding DFT PBE-GGA results on the y-axis with triangular and circular data points from Liu *et al.*[32] and this work, respectively. Fitted lines for E_{ads}^{*N} and E_{ads}^{*O}, and all data points are given in the blue, red, and green dashed lines, respectively.
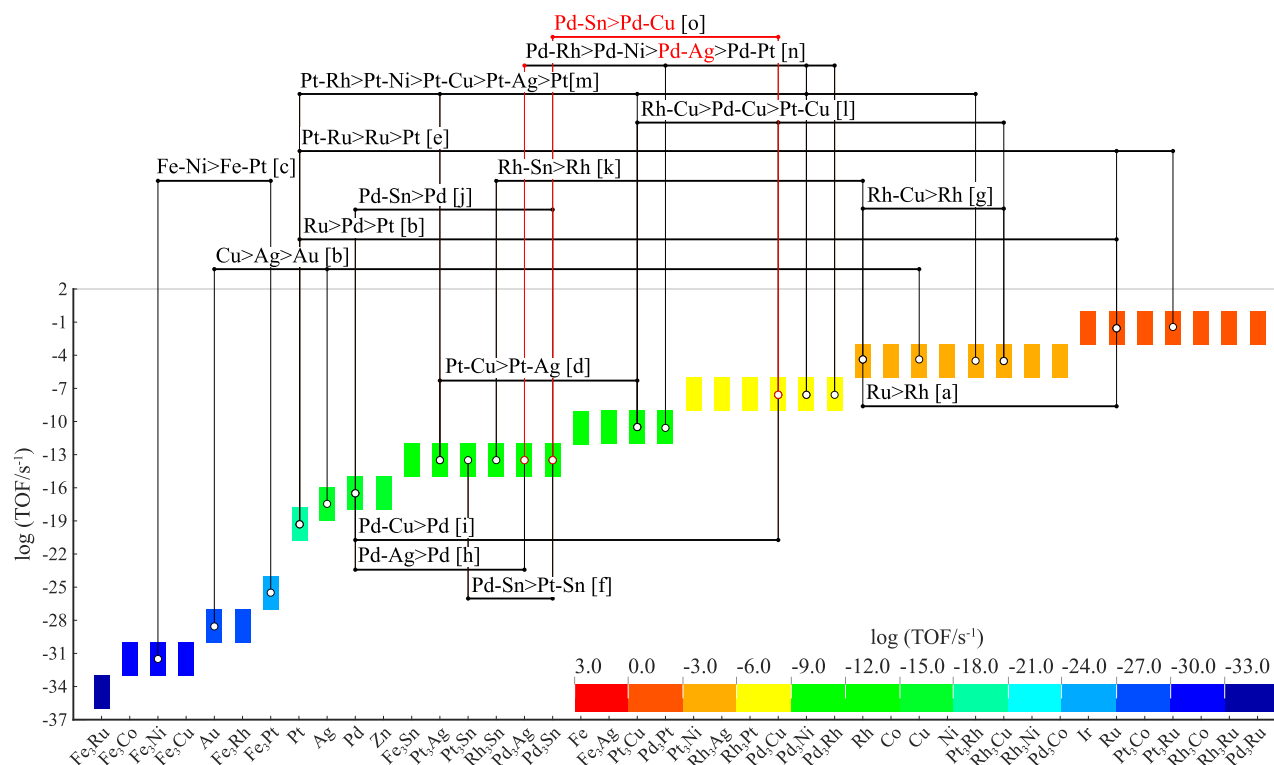
FIG. 2. Plot of the estimated range of TOF obtained from microkinetic modeling by Liu *et al.*[32] The formula of each alloy considered in the study is organized on the x-axis from the lowest to highest range of TOF. Experimental performance trends of different alloys and metals obtained from the available literature are also displayed on top (see references therein). Groups of alloys with trends qualitatively consistent with the work of Liu *et al.*[32] are labeled in black, while alloys with inconsistent trends are labeled in red. (a) Chen *et al.*,[46] (b) Dima, De Vooys, and Koper,[19] (c) Valiyeva *et al.*,[47] (d) Hasnat *et al.*,[48] (e) Wang *et al.*,[33] (f) Hamid, Bae, and Lee,[49] (g) Witońska, Karski, and Gołuchowska,[50] (h) Liu *et al.*,[51] (i) Maia, Rodrigues, and Passos,[52] (j) Park *et al.*,[53] (k) Siriwatcharapiboon *et al.*,[54] (l) Soares, Órfão, and Pereira,[55] (m) Hasnat *et al.*,[48] (n) Hasnat, Karim, and Machida,[56] and (o) Lemaignen *et al.*[57]

and $E_{ads}^{N^*}$ [32] for each material explored in the study. We then annotated the corresponding sets of materials with a ranking of catalytic performance using experimental TOF values when available in the literature and the reported nitrate removal rate when not (see Ref. 2 and references therein).

We note our assessment of computational predictability for experimental catalytic performance comes with additional caveats that must be addressed. First, we acknowledged the experimental rankings in Fig. 2, which were performed under varying conditions (e.g., applied potential, pH, and support materials) derived from varying references. We emphasize that the ranking of different materials presented here is confined to the same experiments and that no comparisons of catalytic performance were done across different references. This will prevent any bias in our ranking that results from the varying experimental conditions while still allowing for a qualitative comparison between the experiment and DFT. Second, we emphasize that although the computational results correspond primarily to binary compositions of A_3B, the experimental results do not necessarily follow the same stoichiometry or crystal structures with some studies focusing on the formation of nanocomposites or doping of metal B. However, the implications of the DFT results

presented by Liu *et al.*[32] was not to predict the catalytic performance of intermetallics with an exact 3:1 ratio. Instead, the purpose was to assess the performance of candidate materials resulting from the synergy between two different metals using a standard crystal structure for ease in comparison. This synergy is possible, regardless of the stoichiometry investigated by Liu *et al.*[32] as demonstrated subsequently in a joint experimental and computational study of Pt–Ru, whereby the same authors identified the optimal stoichiometry to be $Pt_{78}Ru_{22}$.[33]

The majority of trends found from past experiments is qualitatively consistent with the trends for log(TOF) obtained from Liu *et al.*[32] with the exception of the work performed by Lemaignen *et al.*,[57] whereby Pd_3Sn displayed superior catalytic performance over Pd_3Cu experimentally while the computational results demonstrate the opposite. Previous experiments performed by Hasnat, Karim, and Machida[56] have also showed that Pd_3Pt has superior catalytic performance over Pd_3Ag, which is inconsistent with the computed results. Despite the minor discrepancies, the qualitative consistency between the DFT and experimental results for all other trends provides enough confidence to use DFT as a tool for catalyst discovery. We infer by extension, based on the consistency between

DFT and ML shown in Fig. 1, that the ML model is sufficient enough to predict experimentally verifiable trends in activity and can be used to perform large scale screening of electrocatalysts.

D. Modeling catalytic properties

E_{ads}^{O*} and E_{ads}^{N*} can also be used to describe the most probable final by-product of $NO_3^{-1}RR$, i.e., selectivity. We adapted the selectivity maps from Liu et al.[32] in Fig. 4(a) at 0.0 V, Fig. 4(b) at 0.1 V, and Fig. 4(c) at 0.2 V into a single ternary decision map in Fig. 4(d). We specifically highlighted the regions of N_2 (blue) and NH_3 (red) selectivity as N_2 is the desired by-product under the context of water purification, while NH_3 is desired for its chemical utility. For further details about the derivation of Figs. 3 and 4, we direct the reader to the references herein.[32,33]

A model for E_{ads}^{O*} and E_{ads}^{N*} allows us to leverage the activity maps derived by Liu et al.[32] to estimate the turnover frequency (TOF) of NO_3^-RR, the rate of the reaction per surface site [see Figs. 3(a)–3(c)]. Henceforth, we will describe log(TOF) > −3 and
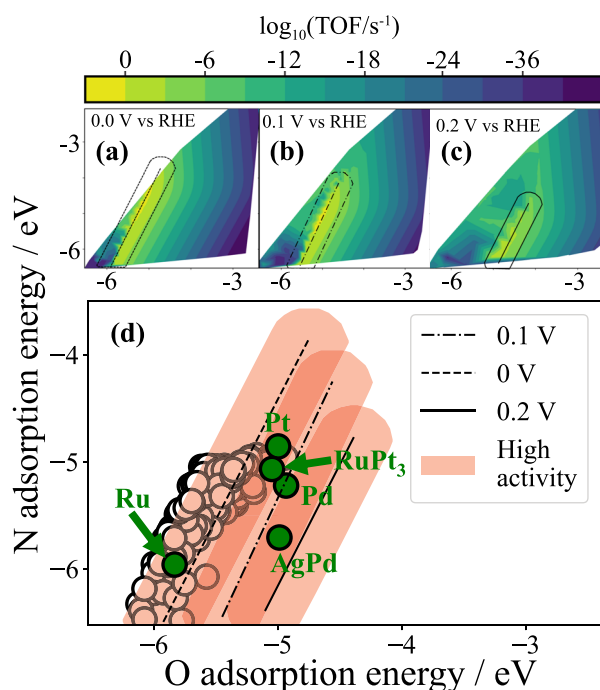

FIG. 3. Theoretical TOF plots as a function of E_{ads}^{O*} (x-axis) and E_{ads}^{N*} (y-axis) for $NO_3^{-1}RR$ derived from Liu et al.[32] under 0.0 V (a), 0.1 V (b), and 0.2 V (c) vs RHE. The region of high activity in each TOF plot (black lines) is represented by Eqs. (B1)–(B3) for (a)–(c), respectively. The activity is simplified to a binary decision map (d) where any surface with a Euclidean distance of 0.3 eV from Eqs. (B1)–(B3) are considered to have high activity (red area). The corresponding individual areas of high activity are also shown in the black oval outline in (a)–(c). ML predicted values for E_{ads}^{O*} and E_{ads}^{N*} using OC20 for the final 20 candidate materials are plotted in (d) as white circles (see Table III for the list of active facets for each material). ML values for a selected number of elemental and intermetallic compounds that exceeded $500/kg in cost but exhibited excellent activity in the literature are also plotted as green circles.
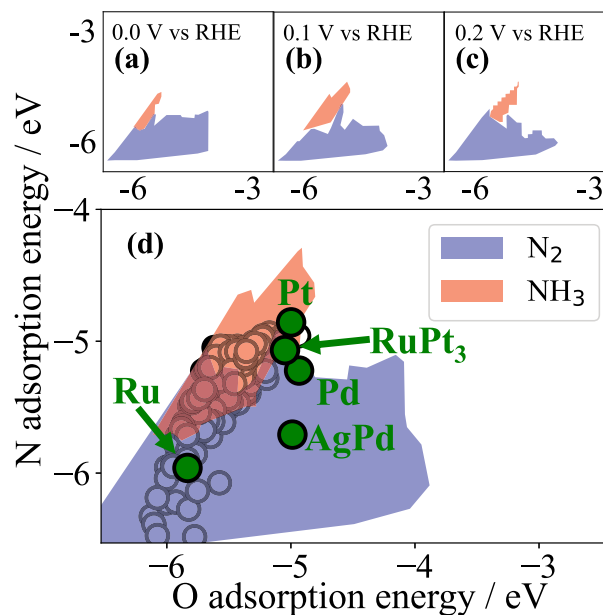

FIG. 4. Binary decision maps for the selectivity of N_2 (blue) and NH_3 (red) as a function of E_{ads}^{O*} (x-axis) and E_{ads}^{N*} (y-axis) derived from Ref. 32. under 0.0 V (a), 0.1 V (b), and 0.2 V (c) vs RHE. Adsorption energies in overlapping areas of red and blue can select NH_3 or N_2 depending on the applied potential. Panel (d) simplifies selectivity by combining (a)–(c) into one overlapping decision map where any data point that falls under it will be considered selective toward N_2, NH_3, or both. ML predicted values for E_{ads}^{O*} and E_{ads}^{N*} using OC20 for the final 20 candidate materials are plotted in (d) as white circles (see Table III for the list of active facets for each material). ML values for a selected number of elemental and intermetallic compounds that exceeded $500/kg in cost but exhibited excellent activity in the literature are also plotted as green circles.

log(TOF) < −3 as high and low activity, respectively. We assessed the NO_3^-RR activity for each bimetallic surface under the applied potentials of 0.0, 0.1, and 0.2 V vs RHE while minding the increase in site competition for hydrogen evolution reactions (HER) at 0.0 V.[32]

III. RESULTS AND DISCUSSION

Figure 5 summarizes the selection criteria that we employed to screen for candidate electrocatalysts. We evaluated all distinct binary intermetallics and ground state elemental crystalline solids reported in the MP and AFLOW databases composed of any combination of the 26 transition metals from Sc to Au, which yielded 59 390 materials (338 binary/unary combinations). Hg and Cd are omitted from the list of metals due to potential toxicity, while Tc is omitted for its radioactivity.

The first criterion describes the Pourbaix stability, i.e., the electrochemical stability of a material in an aqueous environment. We quantify the Pourbaix stability using the Pourbaix decomposition energy (ΔG_{PBX}), which is a function of the applied potential (V) and pH of the environment. Materials with $\Delta G_{PBX} = 0$ eV atom^{-1} are stable under such conditions, while materials with $\Delta G_{PBX} > 0$ eV atom^{-1} are metastable with the likelihood of corrosion increasing with ΔG_{PBX}. It was shown that metastable materials with
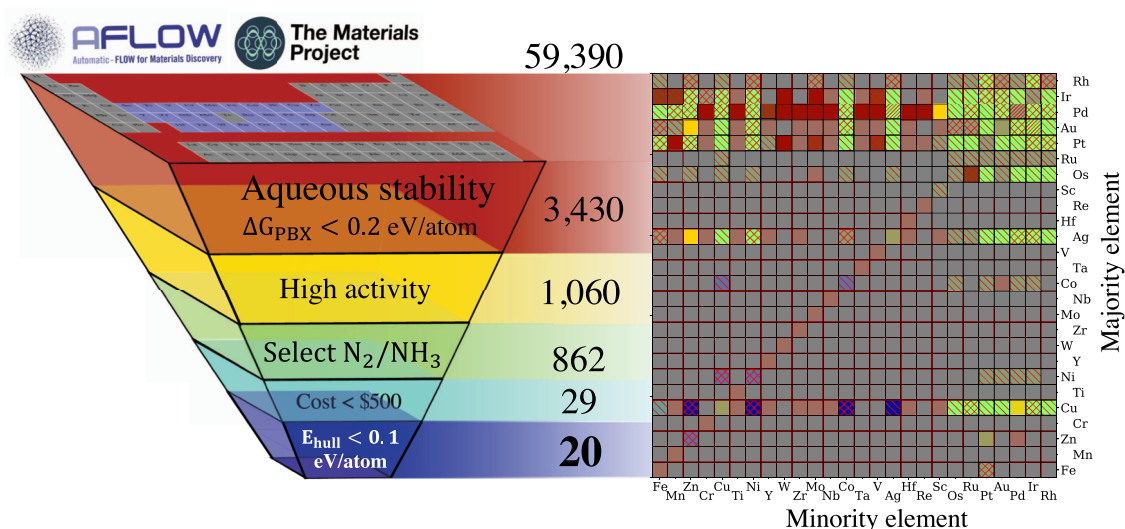
FIG. 5. Selection criteria for NO_3^-RR electrocatalysts with the number of distinct materials that satisfy the current and all prior criteria (left). A periodic table above the first criteria indicates the elements (26 transition metals) considered when screening for bimetallic materials in MP and AFLOW. The selection criteria is accompanied by a grid map for each pair of elements with colors indicating the highest criteria satisfied by any material in that pair composition (right). Grid points on the diagonal correspond to elemental compositions. Shaded grid points correspond to compositions with $0.2 < \Delta G_{PBX} < 0.5$ eV atom^{-1}. Tick labels on the x- and y-axis are sorted from the cheapest (Fe) to the most expensive (Rh) element. Compounds passing the third criteria (selectivity) are designated as selecting N_2 or both N_2 and NH_3 with \ and X hatching, respectively. Elements corresponding to each column (row) in the grid represent minority (majority) species in the compound.

$\Delta G_{PBX} < 0.2$ eV atom^{-1} are less likely to dissolve or corrode in experiments.[61] However, materials with ΔG_{PBX} as high as 0.5 eV atom^{-1} have also been shown to be stable, albeit with many developing passivation layers at the surface, which can inhibit their catalytic capabilities.[62] We allow any material with $\Delta G_{PBX} < 0.2$ eV atom^{-1} at 0.0 V $< V < 0.2$ V and pH = 7 to satisfy this criterion. Due to the exclusive nature of ΔG_{PBX}, only 3430 or 5.78% of the original 59 390 materials (92 out of 338 binary combinations) will satisfy the first criterion with the chemical space confined to materials with a majority/minority composition of Rh, Ir, Pd, Au, Pt, Ru, Os, Ag, or Cu. If we expand our upper limit for ΔG_{PBX} to 0.5 eV atom^{-1}, we find 6971 or 11.74% of the materials (209 out of 338 binary/unary combinations) will satisfy the first criterion (transparent grid points in Fig. 5); however, these materials are more likely to be subject to surface passivation.[62] This criterion will only account for bulk stability under aqueous conditions instead of surface stability. A more accurate assessment of surface stability under aqueous conditions can be performed with the surface Pourbaix diagram, which requires extensive DFT calculations of adsorbed OH, H_2O, O, and H at varying degrees of adsorbate concentration. Bulk Pourbaix stability, although not exact, will at least provide an estimate of aqueous stability across large sets of materials, which to an extent correlates with the relative stability at the surface without the need for expensive adsorption calculations.

The second criterion assesses the activity toward NO_3^{-1}RR of the 3430 materials. A material will satisfy this criterion if any of its surfaces exhibit a data point that lies in the region of high activity shown in Fig. 3(d). Using the IS2RE ML model from the OCP framework (see Sec. II D), we predicted E_{ads}^{O*} and E_{ads}^{N*} for 12 randomly selected surfaces of each of the 3430 candidates. From the adsorption energies, we find that 1060 candidates will satisfy the second criterion (84 binary combinations). Out of the 1060 materials, 308 materials exhibited high activity at an applied potential of 0 V only, at which NO_3^-RR competes with HER. Despite this, we stress that the existence of HER competition does not completely render NO_3^{-1}RR inert. In fact, depending on the applied potential, H^+ can become the dominant product in HER instead of H_2, which can aid in facilitating N_2 selectivity.[15]

Similarly, the third criterion assesses the selectivity toward N_2 of each candidate by plotting the ML values for E_{ads}^{O*} and E_{ads}^{N*} over the decision map shown in Fig. 4(d). We find 862 candidates (67 binary combinations) with data points that lie in the area corresponding to N_2 selectivity, satisfying this criterion. Because of its chemical utility, Fig. 4 also shows the region where selectivity toward NH_3 is favorable. Of the 862 candidates, 811 can select either N_2 or NH_3 depending on the applied potential and facet, allowing for additional utility beyond water purification, while the remaining 51 candidates exclusively select N_2.

The fourth criterion assesses the material cost of each compound in \$/kg/mol. To satisfy this criterion, the cost of a compound must be less than \$500/kg/mol. All metal prices in this study are taken from March 2021.[21,63,64] We note here that the catalytic properties (selectivity and activity), which requires expensive DFT calculations of E_{ads}^{*N} and E_{ads}^{*O}, are assessed prior to our cost criterion. The computational efficiency of our selection criteria should, therefore, account for the cost prior to catalytic properties. However, since our machine learning model allows us to assess E_{ads}^{*N} and E_{ads}^{*O} with negligible computational cost, we elected to assess catalytic properties prior to cost in order to identify potential candidates regardless of material cost. As such, we find that an overwhelming majority of

viable candidates will have varying concentrations of the top seven most expensive metals. By confining materials based on cost, we significantly reduce the number of viable candidates from 862 to 29 (four binary combinations). The remaining binary compounds are Cu-based intermetallics containing Zn, Ni, Co, or Ag. Cu–Fe based components and elemental Zn, Ni, and Co are also viable candidates when the limit for aqueous stability is defined as $\Delta G_{PBX} < 0.5$ eV atom^{-1}.

The fifth and final criterion assesses the thermodynamic stability of the candidate material via the energy above hull (E_{hull}) or the formation energy of a material relative to the ground state. Similar to ΔG_{PBX}, materials with $E_{hull} = 0$ eV atom^{-1} are at the thermodynamic ground state while materials with $E_{hull} > 0$ eV atom^{-1} are metastable with the likelihood of experimental synthesizability decreasing as E_{hull} increases. Materials with a calculated $E_{hull} < 0.1$ eV atom^{-1} have been shown to have reasonable rates of demonstrated synthesis in experiment.[65] We will use this criterion as our final condition for viable catalyst candidates. Of our original 59 390 materials, 20 candidates listed in Table I have passed all five criteria. These candidates, from cheapest to most expensive, are ZnCu$_8$, 6 Cu–Ni alloys, CoCu$_7$, and 12 Cu–Ag alloys. The majority of materials exhibits high activity at an applied potential of 0 V only. All Cu–Ni compounds and two Cu–Ag compounds demonstrate high activity in an applied potential range from 0 to 0.1 V. However, none of the 20 candidates are active at 0.2 V. All candidates can select either N$_2$ or NH$_3$ as a by-product depending on the applied potential and facet except for $C2/m$ Cu$_2$Ag, which exclusively selects N$_2$.

Unsurprisingly, a large majority of compounds predicted to exhibit high turnover frequencies contain noble metals (Rh, Ir, Pd, Au, Pt, Ru, Os, Ag, or Cu), which are known for their resistance to chemical erosion (low ΔG_{PBX}) and excellent catalytic properties

(high TOF).[18,48,56,57] AgPd, in particular, has been known to have the highest reported experimental turnover frequency found so far.[51] From their volcano maps, Liu et al.[32] previously predicted RuPt$_3$ alloys as having excellent catalytic activity, the results of which were subsequently validated in Pt-doped Ru experiments in a separate study.[66] We indeed observed high activity in our ML framework when investigating both Ag–Pd and Ru–Pt alloys (see Fig. 3). However, these components are far too expensive to be commercialized for NO$_3^-$RR. Under a spot price for Pd at \$68 643/kg (accessed from https://www.apmex.com as of 26 June 2020),[64] the cost of Pd catalysts in a trickle reactor will range from \$0.08 to \$1.53 in a catalyst lifespan of 20 to 1 year, respectively. These prices make electrocatalysis economically comparable with ion exchange.[15] With recent price increases in precious metals, the price of Pd has risen to \$79 855/kg (as of 30 April 2021), thus providing no economic advantage over ion exchange. Although Pt and Ru are cheaper than Pd, the volatility of precious metal prices and the risk of price increases exceeding \$68 643/kg in the future makes the long-term economic viability of precious metals unreliable.

Beyond precious metals, we predicted many inexpensive Cu-based compounds to have high activity. Among mono-metallic catalysts, Cu is widely explored in the literature for its relatively high activity for NO$_3^-$RR and has been shown to outperform Pt-group precious metals in regard to activity under acidic conditions.[19,28,67] The activity of Cu surface sites is further enhanced when alloyed with precious metals, such as Pt, Ir, Pd, and Rh,[55,68] as well as common 3d metals, such as Fe, Zn, and Ni,[66,69–72] which is consistent with our predictions (albeit Fe–Cu is shown to have a relatively high aqueous decomposition energy). This stems from the shift in the d-band center of Cu surface sites, which enhances NO$_3$ adsorption. When alloyed with Ni, Cu sites adsorb NO$_3^-$ anions, while Ni

TABLE I. The formula, space group, cost, Pourbaix decomposition energy (at 0.0 and 0.1 V vs RHE), and selectivity of the 20 candidate materials that have satisfied all criteria of our screening process.

Formula	Space group	Cost (\$/kg mol^{-1})	ΔG_{aq} (0.0 V) (eV/atom)	ΔG_{aq} (0.1 V) (eV/atom)	Active at 0.1 V	N$_2$	NH$_3$
ZnCu$_8$	$I4/mmm$	8.78	0.18	0.29	No	✓	✓
Cu$_5$Ni	Cm	10.93	0.15	0.27	Yes	✓	✓
Cu$_5$Ni	$Amm2$	10.93	0.15	0.27	Yes	✓	✓
Cu$_4$Ni	$I4/m$	11.22	0.17	0.29	Yes	✓	✓
Cu$_3$Ni	$R\bar{3}m$	11.65	0.20	0.33	Yes	✓	✓
Cu$_3$Ni	$I4/mmm$	11.65	0.21	0.33	Yes	✓	✓
Cu$_3$Ni	$Cmmm$	11.65	0.21	0.33	Yes	✓	✓
CoCu$_7$	$Fm\bar{3}m$	14.52	0.19	0.30	No	✓	✓
Cu$_4$Ag	$I4/m$	261.58	0.08	0.16	No	✓	✓
Cu$_3$Ag	$P4/mmm$	315.24	0.08	0.15	Yes	✓	✓
Cu$_3$Ag	$Pmmm$	315.24	0.09	0.16	No	✓	✓
Cu$_3$Ag	$Pmmn$	315.24	0.10	0.18	No	✓	✓
Cu$_3$Ag	$C2/m$	315.24	0.10	0.18	Yes	✓	✓
Cu$_3$Ag	$I4/mmm$	315.24	0.10	0.17	No	✓	✓
Cu$_3$Ag	$Pmmn$	315.24	0.10	0.17	No	✓	✓
Cu$_2$Ag	$P6_3/mmc$	397.92	0.07	0.14	No	✓	✓
Cu$_2$Ag	$C2/m$	397.92	0.09	0.15	No	✓	
Cu$_2$Ag	$P6_3/mmc$	397.92	0.07	0.14	No	✓	✓
Cu$_2$Ag	$C2/m$	397.92	0.10	0.17	No	✓	✓
Cu$_5$Ag$_4$	$I4/mmm$	496.75	0.10	0.15	No	✓	✓

sites adsorb H$^+$ to facilitate the successive deoxygenation of NO$_3$* to N*.[73]

Although many of the intermetallic alloys screened considered in this study were not stable in an aqueous environment, it is reasonable that these synergistic effects can be achieved when alloying Cu with other inexpensive metals via surface doping as has been shown in many experimental studies to produce an effective and economical electrocatalyst. Our findings also demonstrate that the catalytic viability of Cu–Ag and Cu–Ni candidates are insensitive to composition and structure as shown by the diversity of such materials reported in Table I, which makes surface doping of Cu with Ag or Ni a possible approach to create an electrocatalyst.

As far as the authors are aware, Cu–Co and Cu–Ag compounds have yet to be explored as electrocatalysts for NO$_3^-$RR in the literature.

Given that the purpose of our work was to identify promising catalysts based on criteria that could be rapidly assessed for thousands of candidate materials, we have naturally had to neglect several factors that will be critical to the further development of a practical nitrate reduction electrocatalyst for water purification. First, our screening assumed that all reactions occurred under a neutral pH as N$_2$ production became more favorable at pH > 4.[74–77] Furthermore, in the context of water purification, many groundwater sources have near-neutral pH (e.g., 6–8), and it is generally desirable to minimize pH adjustment since it entails costly additional chemical handling.[15,78] Hence, evaluating catalyst performance at neutral pH is a sensible starting point.

Second, our computational methods did not capture the effects of solvation or competition by ubiquitous environmental ions nor did they account for the effect of the electrolyte. Common ions, such as Cl$^-$, Br$^-$, SO$_4^{-2}$, and PO$_4^{-3}$, have been shown to affect the activity and selectivity of NO$_3^-$RR in both passive reduction on zero-valent iron and electroreduction.[74,79] This is especially important in the context of water purification where nitrate runoff may enter natural waters containing background electrolytes such as NaCl and Na$_2$SO$_4$. Chloride and sulfate anions, in particular, have been shown to decrease catalytic activity by poisoning and dissolving the catalyst.[80]

Despite this, both Liu *et al.*[32] and this study (see Fig. 2) have been able to approximate past experimental trends in activity using the microkinetic models. Furthermore, scaling relationships used to develop volcano maps are known to generalize models beyond single adsorbates on slabs, including solid–liquid interfaces, which shift the adsorption energy by a constant value.[81,82] Finally, microkinetic simulations of adsorbate coverage demonstrate H* and NO$_3^-$* to be the dominant competing species under negative and positive potentials, respectively; however, additional simulations of adsorption for common solvents and electrolytes are required to gauge their competitiveness with H* and NO$_3^-$*. Furthermore, accurately modeling electrolyte and solvation effects would require substantial additional computational effort. At a minimum, it would be necessary to perform DFT calculations of co-adsorption of NO$_3^-$RR intermediates with the aforementioned anions at varying concentrations of an implicit solvent. Higher accuracy could be obtained by calculating a liquid interface with the catalyst surface, which can be used to model an electrolyte interface or an explicit solvent but requires costly *ab initio* molecular dynamics simulations. However, both the OC20 framework and the microkinetic models developed by Liu *et al.*[32] used in this study are limited to single intermediate adsorption on a catalyst surface under a vacuum interface.

Finally, since our screening criteria were based on thermodynamics, we did not estimate the overpotentials of our proposed materials or directly determine their turnover frequencies via, e.g., transition state calculations. Both factors will have an important impact on the ultimate economic viability of the electrocatalyst.

Despite the simplifications required by the scale of our screening (50 000 + materials), by identifying a small number of promising candidates, this work will facilitate more sophisticated simulations and experiments that can further evaluate the factors discussed above.

IV. CONCLUSION

By coupling machine learning with previous scaling relationships for NO$_3^-$RR, we developed an efficient and computationally inexpensive screening strategy that revealed 20 economically viable electrocatalysts out of an initial pool of more than 50 000 candidates. The majority of candidate materials are Cu-based intermetallics owing to the excellent activity of Cu and its synergistic effect with other transition metals. Most of the candidates can select either N$_2$ or NH$_3$, depending on the applied potential and facet, giving it utility in water purification as well as NH$_3$ production. We performed DFT calculations to verify the ML adsorption energies of a select number of viable catalytic materials, most of which demonstrated adsorption energies within or adjacent to the areas of high activity. The catalytically active compounds exhibited in our grid map of binary intermetallics (Fig. 5) contain precious metals as well as Cu, which is in agreement with previous studies. Future studies will explicitly calculate the reaction pathways and transition states of the materials proposed herein as well as experimentally validate their catalytic activity toward NO$_3^-$RR.

AUTHOR DECLARATIONS

Conflict of Interest

The authors have no conflicts to disclose.

Author Contributions

Richard Tran: Data curation (equal); Formal analysis (lead); Methodology (equal); Validation (equal); Visualization (equal); Writing – original draft (lead); Writing – review & editing (lead). **Duo Wang:** Data curation (equal); Formal analysis (supporting); Validation (equal); Visualization (equal); Writing – original draft (supporting); Writing – review & editing (supporting). **Ryan Kingsbury:** Conceptualization (supporting); Formal analysis (supporting); Validation (supporting); Writing – original draft (supporting); Writing – review & editing (supporting). **Aini Palizhati:** Software (supporting). **Kristin Aslaug Persson:** Resources (supporting); Supervision (supporting). **Anubhav Jain:** Funding acquisition (equal); Project administration (equal); Resources (equal); Supervision (supporting); Writing – original draft (supporting); Writing – review & editing (supporting). **Zachary W. Ulissi:** Funding acquisition (equal); Project administration (equal); Supervision (lead); Writing – original draft (supporting); Writing – review & editing (supporting).

DATA AVAILABILITY

The data that support the findings of this study are openly available in Github repository.[83] All datasets used in training the ML model are publicly available (OC20[34]).

APPENDIX A: POURBAIX DECOMPOSITION

All candidates identified are metastable under aqueous conditions with a $\Delta G_{PBX} < 0.2$ eV/atom. The candidate catalyst can either dissolve into ionic components or the surface can be passivated into a solid listed in Table II depending on factors such as temperature, solvation, or pressure.

APPENDIX B: ACTIVITY AND SELECTIVITY DECISION MAPS

To determine the area on the maps corresponding to high activity [log(TOF) > −3], we approximated a line of high activity for each heat map that lies on the center of the warmest region of the map [see Figs. 3(a)–3(c)] given by

$$E_{ads}^{N^*} = 2.27 E_{ads}^{O^*} + 6.95, \left\{ E_{ads}^{O^*} : -5.90 < E_{ads}^{O^*} < -5.13 \right\}, \quad (B1)$$

$$E_{ads}^{N^*} = 2.44 E_{ads}^{O^*} + 7.21, \left\{ E_{ads}^{O^*} : -5.30 < E_{ads}^{O^*} < -4.85 \right\}, \quad (B2)$$

TABLE II. The ground state components that four binary compositions can decompose into under pH = 7 and an applied potential of 0.0 and 0.1 V.

	0.0 V	0.1 V
Zn–Cu	$Zn^{+2} + Cu^{+1}$	$CuO(s) + Zn^{+2}$
Ni–Cu	$Ni^{+2} + Cu^{+1}$	$Ni^{+2} + CuO(s)$
Ag–Cu	$Ag(s) + Cu^{+1}$	$Ag(s) + CuO(s)$
Co–Cu	$Cu^{+1} + Co^{+2}$	$Co^{+2} + CuO(s)$

$$E_{ads}^{N^*} = 2.27 E_{ads}^{O^*} + 5.17, \left\{ E_{ads}^{O^*} : -5.10 < E_{ads}^{O^*} < -4.39 \right\}, \quad (B3)$$

with Eqs. S1–S3 corresponding to 0.0, 0.1, and 0.2 V vs RHE, respectively. The MAE of the ML model developed by Chanussot et al.[34] is ~0.3 eV. As such, we consider a buffer distance of 0.3 eV from

TABLE III. The Miller indices listed in the third column correspond to the facets with high activity and N_2 selectivity. The tabulated data for price, Pourbaix decomposition energy, activity, and selectivity can be found in Table I.

Formula	Space group	Miller indices (hkl)
ZnCu_8	$I4/mmm$	$(443), (334), (331)$
Cu_5Ni	Cm	$(24\bar{3}), (21\bar{2}), (21\bar{3}), (40\bar{3}), (20\bar{3}), (30\bar{1})$ $(103), (21\bar{4}), (23\bar{4}), (234), (40\bar{1}), (30\bar{2})$
Cu_5Ni	$Amm2$	$(334), (233), (041), (032), (031), (012)$ $(023), (013), (124), (114), (104)$
Cu_4Ni	$I4/m$	$(221), (320), (310), (223), (430)$ $(212), (410), (201), (334), (331)$
Cu_3Ni	$R\bar{3}m$	$(10\bar{3}), (10\bar{4}), (103), (104), (4\bar{1}0), (4\bar{1}4)$ $(2\bar{1}2), (32\bar{3}), (320), (4\bar{1}\bar{4}), (10\bar{2}), (102)$
Cu_3Ni	$I4/mmm$	$(103), (430), (211), (210), (414), (410)$ $(320), (313), (310), (112), (102), (113)$
Cu_3Ni	$Cmmm$	$(120), (221), (124), (201), (243), (320)$ $(121), (140), (210), (233), (341), (441)$
CoCu_7	$Fm\bar{3}m$	$(221), (332), (331)$
Cu_4Ag	$I4/m$	$(221), (212), (423), (334), (223), (213)$
Cu_3Ag	$P4/mmm$	$(210), (213), (114)$
Cu_3Ag	$Pmmm$	$(120), (223), (124), (113)$
Cu_3Ag	$Pmmn$	$(143), (132), (124), (123)$ $(113), (243), (423)$
Cu_3Ag	$C2/m$	$(114), (12\bar{3}), (113), (123), (223), (12\bar{4})$ $(13\bar{4}), (134), (214), (23\bar{4}), (234), (33\bar{4})$
Cu_3Ag	$I4/mmm$	$(334), (324), (223), (213)$
Cu_3Ag	$Pmmn$	$(124), (123), (203)$
Cu_2Ag	$P6_3/mmc$	$(3\bar{3}\bar{6}4), (30\bar{3}4), (10\bar{1}2), (20\bar{2}3), (10\bar{1}3)$
Cu_2Ag	$C2/m$	$(323), (23\bar{4}), (11\bar{2}), (21\bar{4})$ $(423), (211), (21\bar{2}), (114)$
Cu_2Ag	$P6_3/mmc$	$(10\bar{1}2), (10\bar{1}4), (10\bar{1}3)$
Cu_2Ag	$C2/m$	$(11\bar{2}), (11\bar{3}), (31\bar{3}), (11\bar{4}), (114), (12\bar{3})$ $(123), (21\bar{4}), (22\bar{3}), (223), (323), (23\bar{4})$
Cu_5Ag_4	$I4/mmm$	$(331), (443)$

Eqs. S1–S3 as potential regions of high activity, which yields an ellipse around the corresponding line. The areas within the three ellipses (red) are considered regions of high activity, whereas areas outside the ellipsis will have low activity.

APPENDIX C: FACETS OF CANDIDATE MATERIALS

Table III lists the formula, space group, and facet Miller indices of the 20 candidate materials that have satisfied all criteria of our screening process.

REFERENCES

[1] D. Xu, Y. Li, L. Yin, Y. Ji, J. Niu, and Y. Yu, "Electrochemical removal of nitrate in industrial wastewater," Front. Environ. Sci. Eng. **12**, 9 (2018).

[2] R. Carrey, E. Ballesté, A. R. Blanch, F. Lucena, P. Pons, J. M. López, M. Rull, J. Solà, N. Micola, J. Fraile et al., "Combining multi-isotopic and molecular source tracking methods to identify nitrate pollution sources in surface and groundwater," Water Res. **188**, 116537 (2021).

[3] Q. Yi, Y. Zhang, K. Xie, Q. Chen, F. Zheng, D. Tonina, W. Shi, and C. Chen, "Tracking nitrogen pollution sources in plain watersheds by combining high-frequency water quality monitoring with tracing dual nitrate isotopes," J. Hydrol. **581**, 124439 (2020).

[4] P. M. Vitousek, J. D. Aber, R. W. Howarth, G. E. Likens, P. A. Matson, D. W. Schindler, W. H. Schlesinger, and D. G. Tilman, "Human alteration of the global nitrogen cycle: Sources and consequences," Ecol. Appl. **7**, 737–750 (1997).

[5] R. Epsztein, O. Nir, O. Lahav, and M. Green, "Selective nitrate removal from groundwater using a hybrid nanofiltration–reverse osmosis filtration scheme," Chem. Eng. J. **279**, 372–378 (2015).

[6] L. N. Pincus, H. E. Rudel, P. V. Petrović, S. Gupta, P. Westerhoff, C. L. Muhich, and J. B. Zimmerman, "Exploring the mechanisms of selectivity for environmentally significant oxo-anion removal during water treatment: A review of common competing oxo-anions and tools for quantifying selective adsorption," Environ. Sci. Technol. **54**, 9769–9790 (2020).

[7] S. Samatya, N. Kabay, Ü. Yüksel, M. Arda, and M. Yüksel, "Removal of nitrate from aqueous solution by nitrate selective ion exchange resins," React. Funct. Polym. **66**, 1206–1214 (2006).

[8] G. K. Luk and W. C. Au-Yeung, "Experimental investigation on the chemical reduction of nitrate from groundwater," Adv. Environ. Res. **6**, 441–453 (2002).

[9] S. Guo, K. Heck, S. Kasiraju, H. Qian, Z. Zhao, L. C. Grabow, J. T. Miller, and M. S. Wong, "Insights into nitrate reduction over indium-decorated palladium nanoparticle catalysts," ACS Catal. **8**, 503–515 (2018).

[10] J. Radjenovic and D. L. Sedlak, "Challenges and opportunities for electrochemical processes as next-generation technologies for the treatment of contaminated water," Environ. Sci. Technol. **49**, 11292–11302 (2015).

[11] M. I. M. Soares, "Biological denitrification of groundwater," Water, Air, Soil Pollut. **123**, 183–193 (2000).

[12] P. M. Ayyasamy, K. Shanthi, P. Lakshmanaperumalsamy, S.-J. Lee, N.-C. Choi, and D.-J. Kim, "Two-stage removal of nitrate from groundwater using biological and chemical treatments," J. Biosci. Bioeng. **104**, 129–134 (2007).

[13] F. Rezvani, M.-H. Sarrafzadeh, S. Ebrahimi, and H.-M. Oh, "Nitrate removal from drinking water with a focus on biological methods: A review," Environ. Sci. Pollut. Res. **26**, 1124–1141 (2019).

[14] J. L. Schnoor, Salt: The Final Frontier (ACS Publications, 2013).

[15] C. J. Werth, C. Yan, and J. P. Troutman, "Factors impeding replacement of ion exchange with (electro)catalytic treatment for nitrate removal from drinking water," ACS EST Eng. **1**, 6–20 (2021).

[16] W. Duan, G. Li, Z. Lei, T. Zhu, Y. Xue, C. Wei, and C. Feng, "Highly active and durable carbon electrocatalyst for nitrate reduction reaction," Water Res. **161**, 126–135 (2019).

[17] M. Paidar, I. Roušar, and K. Bouzek, "Electrochemical removal of nitrate ions in waste solutions after regeneration of ion exchange columns," J. Appl. Electrochem. **29**, 611–617 (1999).

[18] J. Martínez, A. Ortiz, and I. Ortiz, "State-of-the-art and perspectives of the catalytic and electrocatalytic reduction of aqueous nitrates," Appl. Catal., B **207**, 42–59 (2017).

[19] G. E. Dima, A. C. A. De Vooys, and M. T. M. Koper, "Electrocatalytic reduction of nitrate at low concentration on coinage and transition-metal electrodes in acid solutions," J. Electroanal. Chem. **554–555**, 15–23 (2003).

[20] Z. Shen, D. Liu, G. Peng, Y. Ma, J. Li, J. Shi, J. Peng, and L. Ding, "Electrocatalytic reduction of nitrate in water using Cu/Pd modified Ni foam cathode: High nitrate removal efficiency and N_2-selectivity," Sep. Purif. Technol. **241**, 116743 (2020).

[21] Metalary—Latest and Historical Metal Prices, www.metalary.com, 2016.

[22] A. K. Singh, J. H. Montoya, J. M. Gregoire, and K. A. Persson, "Robust and synthesizable photocatalysts for CO_2 reduction: A data-driven materials discovery," Nat. Commun. **10**, 443 (2019).

[23] K. Abdelfatah, W. Yang, R. Vijay Solomon, A. Rajbanshi, A. Chowdhury, M. Zare, S. K. Kundu, A. Yonge, A. Heyden, and G. Terejanu, "Prediction of transition-state energies of hydrodeoxygenation reactions on transition-metal surfaces based on machine learning," J. Phys. Chem. C **123**, 29804–29810 (2019).

[24] D. Roy, S. C. Mandal, and B. Pathak, "Machine learning-driven high-throughput screening of alloy-based catalysts for selective CO_2 hydrogenation to methanol," ACS Appl. Mater. Interfaces **13**, 56151 (2021).

[25] A. Malek, Q. Wang, S. Baumann, O. Guillon, M. Eikerling, and K. Malek, "A data-driven framework for the accelerated discovery of CO_2 reduction electrocatalysts," Front. Energy Res. **9**, 609070 (2021).

[26] G. H. Gu, J. Noh, S. Kim, S. Back, Z. Ulissi, and Y. Jung, "Practical deep-learning representation for fast heterogeneous catalyst screening," J. Phys. Chem. Lett. **11**, 3185–3191 (2020).

[27] J. Schumann, A. J. Medford, J. S. Yoo, Z.-J. Zhao, P. Bothra, A. Cao, F. Studt, F. Abild-Pedersen, and J. K. Nørskov, "Selectivity of synthesis gas conversion to C_{2+} oxygenates on fcc(111) transition-metal surfaces," ACS Catal. **8**, 3447–3453 (2018).

[28] T. Wang, G. Li, X. Cui, and F. Abild-Pedersen, "Identification of earth-abundant materials for selective dehydrogenation of light alkanes to olefins," Proc. Natl. Acad. Sci. U. S. A. **118**, e2024666118 (2021).

[29] S. Wang, N. Omidvar, E. Marx, and H. Xin, "Coordination numbers for unraveling intrinsic size effects in gold-catalyzed CO oxidation," Phys. Chem. Chem. Phys. **20**, 6055–6059 (2018).

[30] Y. Song and L. C. Grabow, "Activity trends for catalytic CO and NO Co-oxidation at low temperature diesel emission conditions," Ind. Eng. Chem. Res. **57**, 12715–12725 (2018).

[31] K. S. Exner, I. Sohrabnejad-Eskan, and H. Over, "A universal approach to determine the free energy diagram of an electrocatalytic reaction," ACS Catal. **8**, 1864–1879 (2018).

[32] J.-X. Liu, D. Richards, N. Singh, and B. R. Goldsmith, "Activity and selectivity trends in electrocatalytic nitrate reduction on transition metals," ACS Catal. **9**, 7052–7064 (2019).

[33] Z. Wang, S. D. Young, B. R. Goldsmith, and N. Singh, "Increasing electrocatalytic nitrate reduction activity by controlling adsorption through PtRu alloying," J. Catal. **395**, 143–154 (2021).

[34] L. Chanussot, A. Das, S. Goyal, T. Lavril, M. Shuaibi, M. Riviere, K. Tran, J. Heras-Domingo, C. Ho, W. Hu, A. Palizhati, A. Sriram, B. Wood, J. Yoon, D. Parikh, C. L. Zitnick, and Z. Ulissi, "Open catalyst 2020 (OC20) dataset and community challenges," ACS Catal. **11**, 6059–6072 (2021); arXiv:2010.09990.

[35] W. L. Hamilton, R. Ying, and J. Leskovec, "Representation learning on graphs: Methods and applications," in IEEE Data Engineering Bulletin, 2017.

[36] A. Jain, S. P. Ong, G. Hautier, W. Chen, W. D. Richards, S. Dacek, S. Cholia, D. Gunter, D. Skinner, G. Ceder et al., "Commentary: The materials project: A materials genome approach to accelerating materials innovation," APL Mater. **1**, 011002 (2013).

[37] S. Curtarolo, W. Setyawan, G. L. W. Hart, M. Jahnatek, R. V. Chepulskii, R. H. Taylor, S. Wang, J. Xue, K. Yang, O. Levy et al., "AFLOW: An automatic framework for high-throughput materials discovery," Comput. Mater. Sci. **58**, 218–226 (2012).

[38] J. H. Montoya and K. A. Persson, "A high-throughput framework for determining adsorption energies on solid surfaces," npj Comput. Mater. **3**, 14 (2017).

[39] G. Kresse and J. Furthmüller, "Efficient iterative schemes for *ab initio* total-energy calculations using a plane-wave basis set," Phys. Rev. B **54**, 11169–11186 (1996).

[40] G. Kresse and J. Hafner, "*Ab initio* molecular dynamics for liquid metals," Phys. Rev. B **47**, 558–561 (1993).

[41] P. E. Blöchl, "Projector augmented-wave method," Phys. Rev. B **50**, 17953–17979 (1994).

[42] J. P. Perdew, K. Burke, and M. Ernzerhof, "Generalized gradient approximation made simple," Phys. Rev. Lett. **77**, 3865–3868 (1996).

[43] M. Methfessel and A. T. Paxton, "High-precision sampling for Brillouin-zone integration in metals," Phys. Rev. B **40**, 3616–3621 (1989).

[44] S. P. Ong, W. D. Richards, A. Jain, G. Hautier, M. Kocher, S. Cholia, D. Gunter, V. L. Chevrier, K. A. Persson, and G. Ceder, "Python materials Genomics (pymatgen): A robust, open-source python library for materials analysis," Comput. Mater. Sci. **68**, 314–319 (2013).

[45] W. Sun and G. Ceder, "Efficient creation and convergence of surface slabs," Surf. Sci. **617**, 53–59 (2013).

[46] X. Chen, X. Huo, J. Liu, Y. Wang, C. J. Werth, and T. J. Strathmann, "Exploring beyond palladium: Catalytic reduction of aqueous oxyanion pollutants with alternative platinum group metals and new mechanistic implications," Chem. Eng. J. **313**, 745–752 (2017).

[47] G. G. Valiyeva, I. Bavasso, L. Di Palma, S. R. Hajiyeva, M. A. Ramazanov, and F. V. Hajiyeva, "Synthesis of Fe/Ni bimetallic nanoparticles and application to the catalytic removal of nitrates from water," Nanomaterials **9**, 1130 (2019).

[48] M. A. Hasnat, R. Agui, S. Hinokuma, T. Yamaguchi, and M. Machida, "Different reaction routes in electrocatalytic nitrate/nitrite reduction using an H^+-conducting solid polymer electrolyte," Catal. Commun. **10**, 1132–1135 (2009).

[49] S. Hamid, S. Bae, and W. Lee, "Novel bimetallic catalyst supported by red mud for enhanced nitrate reduction," Chem. Eng. J. **348**, 877–887 (2018).

[50] I. Witońska, S. Karski, and J. Gołuchowska, "Kinetic studies on the hydrogenation of nitrate in water using Rh/Al$_2$O$_3$ and Rh–Cu/Al$_2$O$_3$ catalysts," Kinet. Catal. **48**, 823–828 (2007).

[51] H. Liu, Y. Yu, W. Yang, W. Lei, M. Gao, and S. Guo, "High-density defects on PdAg nanowire networks as catalytic hot spots for efficient dehydrogenation of formic acid and reduction of nitrate," Nanoscale **9**, 9305–9309 (2017).

[52] M. P. Maia, M. A. Rodrigues, and F. B. Passos, "Nitrate catalytic reduction in water using niobia supported palladium–copper catalysts," Catal. Today **123**, 171–176 (2007).

[53] J. Park, J. K. Choe, W. Lee, and S. Bae, "Highly fast and selective removal of nitrate in groundwater by bimetallic catalysts supported by fly ash-derived zeolite Na-X," Environ. Sci.: Nano **7**, 3360–3371 (2020).

[54] W. Siriwatcharapiboon, Y. Kwon, J. Yang, R. L. Chantry, Z. Li, S. L. Horswell, and M. T. M. Koper, "Promotion effects of Sn on the electrocatalytic reduction of nitrate at Rh nanoparticles," ChemElectroChem **1**, 172–179 (2014).

[55] O. S. G. P. Soares, J. J. M. Órfão, and M. F. R. Pereira, "Bimetallic catalysts supported on activated carbon for the nitrate reduction in water: Optimization of catalysts composition," Appl. Catal., B **91**, 441–448 (2009).

[56] M. A. Hasnat, M. R. Karim, and M. Machida, "Electrocatalytic ammonia synthesis: Role of cathode materials and reactor configuration," Catal. Commun. **10**, 1975–1979 (2009).

[57] L. Lemaignen, C. Tong, V. Begon, R. Burch, and D. Chadwick, "Catalytic denitrification of water with palladium-based catalysts supported on activated carbons," Catal. Today **75**, 43–48 (2002).

[58] J. Klicpera, S. Giri, J. T. Margraf, and S. Günnemann, "Fast and uncertainty-aware directional message passing for non-equilibrium molecules," arXiv:2011.14115 (2020).

[59] J. Klicpera, J. Groß, and S. Günnemann, "Directional message passing for molecular graphs," in *International Conference on Learning Representations (ICLR)* (ICLR, 2020), pp. 1–13.

[60] A. J. R. Hensley, K. Ghale, C. Rieg, T. Dang, E. S. Anderst, F. Studt, C. T. Campbell, J.-S. McEwen, and Y. Xu, "A DFT-based method for more accurate adsorption energies: An adaptive sum of energies from RPBE and vdW density functionals," J. Phys. Chem. C **121**, 4937 (2017).

[61] A. Jain, Z. Wang, and J. K. Nørskov, "Stable two-dimensional materials for oxygen reduction and oxygen evolution reactions," ACS Energy Lett. **4**, 1410–1411 (2019).

[62] A. K. Singh, L. Zhou, A. Shinde, S. K. Suram, J. H. Montoya, D. Winston, J. M. Gregoire, and K. A. Persson, "Electrochemical stability of metastable materials," Chem. Mater. **29**, 10159–10167 (2017).

[63] Daily Metal Price: Free Metal Price Tables and Charts, https://www.dailymetalprice.com/, 2021.

[64] APMEX: Precious Metals Dealer, https://www.apmex.com/, 2021.

[65] M. Aykol, S. S. Dwaraknath, W. Sun, and K. A. Persson, "Thermodynamic limit for synthesis of metastable inorganic materials," Sci. Adv. **4**, eaaq0148 (2018).

[66] Y. Wang, A. Xu, Z. Wang, L. Huang, J. Li, F. Li, J. Wicks, M. Luo, D.-H. Nam, C.-S. Tan, Y. Ding, J. Wu, Y. Lum, C.-T. Dinh, D. Sinton, G. Zheng, and E. H. Sargent, "Enhanced nitrate-to-ammonia activity on copper-nickel alloys via tuning of intermediate adsorption," J. Am. Chem. Soc. **142**, 5702–5708 (2020).

[67] X. Zhang, Y. Wang, C. Liu, Y. Yu, S. Lu, and B. Zhang, "Recent advances in non-noble metal electrocatalysts for nitrate reduction," Chem. Eng. J. **403**, 126269 (2021).

[68] N. Comisso, S. Cattarin, S. Fiameni, R. Gerbasi, M. Mattarozzi, M. Musiani, L. Vázquez-Gómez, and E. Verlato, "Electrodeposition of Cu-Rh alloys and their use as cathodes for nitrate reduction," Electrochem. Commun. **25**, 91–93 (2012).

[69] Y. Zhang, Y. Zhao, Z. Chen, L. Wang, L. Zhou, P. Wu, F. Wang, and P. Ou, "Fe/Cu composite electrode prepared by electrodeposition and its excellent behavior in nitrate electrochemical removal," J. Electrochem. Soci. **165**, E420–E428 (2018).

[70] L. Mattarozzi, S. Cattarin, N. Comisso, R. Gerbasi, P. Guerriero, M. Musiani, L. Vázquez-Gómez, and E. Verlato, "Electrodeposition of compact and porous Cu-Zn alloy electrodes and their use in the cathodic reduction of nitrate," J. Electrochem. Soc. **162**, D236–D241 (2015).

[71] L. Mattarozzi, S. Cattarin, N. Comisso, P. Guerriero, M. Musiani, L. Vázquez-Gómez, and E. Verlato, "Electrochemical reduction of nitrate and nitrite in alkaline media at CuNi alloy electrodes," Electrochim. Acta **89**, 488–496 (2013).

[72] D. Reyter, D. Bélanger, and L. Roué, "Optimization of the cathode material for nitrate removal by a paired electrolysis process," J. Hazard. Mater. **192**, 507–513 (2011).

[73] B. K. Simpson and D. C. Johnson, "Electrocatalysis of nitrate reduction at copper-nickel alloy electrodes in acidic media," Electroanalysis **16**, 532–538 (2004).

[74] Y. Zeng, C. Priest, G. Wang, and G. Wu, "Restoring the nitrogen cycle by electrochemical reduction of nitrate: Progress and prospects," Small Methods **4**, 2000672 (2020).

[75] Z. Wang, D. Richards, and N. Singh, "Recent discoveries in the reaction mechanism of heterogeneous electrocatalytic nitrate reduction," Catal.: Sci. Technol. **11**, 705–725 (2021).

[76] J. M. McEnaney, S. J. Blair, A. C. Nielander, J. A. Schwalbe, D. M. Koshy, M. Cargnello, and T. F. Jaramillo, "Electrolyte engineering for efficient electrochemical nitrate reduction to ammonia on a titanium electrode," ACS Sustainable Chem. Eng. **8**, 2672–2681 (2020).

[77] M. T. De Groot and M. T. M. Koper, "The influence of nitrate concentration and acidity on the electrocatalytic reduction of nitrate on platinum," J. Electroanal. Chem. **562**, 81–94 (2004).

[78] C. Bing, Bureau of Reclamation, 2009.

[79] C. Su and R. W. Puls, "Nitrate reduction by zerovalent iron: Effects of formate, oxalate, citrate, chloride, sulfate, borate, and phosphate," Environ. Sci. Technol. **38**, 2715–2720 (2004).

[80] M. A. Hasnat, J. A. Safwan, M. A. Rashed, Z. Rahman, M. M. Rahman, Y. Nagao, and A. M. Asiri, "Inverse effects of supporting electrolytes on the electrocatalytic nitrate reduction activities in a Pt|Nafion|Pt-Cu-type reactor assembly," RSC Adv. **6**, 11609–11617 (2016).

[81] A. Kulkarni, S. Siahrostami, A. Patel, and J. K. Nørskov, "Understanding catalytic activity trends in the oxygen reduction reaction," Chem. Rev. **118**, 2302–2312 (2018).

[82] J. K. Nørskov, F. Studt, F. Abild-Pederson, and T. Bligaard, *Fundamental Concepts in Heterogeneous Catalysis* (John Wiley & Sons, Hoboken, NJ, 2014), p. 196.

[83] Nitrate https://github.com/ulissigroup/nitrate, 2021.